Design, Synthesis and Properties

BARIUM TITANATE STANNATE FUNCTIONALLY GRADED MATERIALS: CHOOSING OF THE Ti/Sn CONCENTRATION GRADIENT AND THE INFLUENCE OF THE GRADIENT ON ELECTRICAL PROPERTIES

S. Marković and D. Uskoković
Institute of Technical Sciences of the Serbian Academy of Sciences and Arts,
Belgrade, Serbia

ABSTRACT

Barium titanate stannate ($BaTi_{1-x}Sn_xO_3$, BTS) functionally graded materials (FGMs) with different Ti/Sn concentration gradients were prepared by the powder processing method followed by sintering. Firstly, with the aim of tailoring the concentration gradient of Ti/Sn, the main characteristics of BTS ingredients were studied. The influence of the Ti/Sn concentration gradient on the electrical characteristics of the FGMs was examined by impedance spectroscopy (*IS*). The grain-interior and grain boundary resistivity of the FGMs were distinguished and activation energies were calculated. It has been established that for the FGMs the activation energy deduced from the grain-interior conductivity (0.74–0.78 eV) is defined by chemical composition (intrinsic property) and that it does not depend on the Ti/Sn concentration gradient. Quite contrary, the activation energy for the grain boundary conductivity (1.03–1.29 eV) is determined by the microstructural gradient which is a direct consequence of the concentration gradient. The results of *IS* indicate that there are no insulator interfaces (cracks and/or delamination) between graded layers in FGMs. This assumption was confirmed by *in situ* monitoring of the sintering processes in thermal microscope, and furthermore, by SEM analysis of FGMs in cross-sectional view.

INTRODUCTION

Emerging technologies are demanding new materials with electrical and/or magnetic multifunctional properties, enhancing structural performances, such as mechanical and thermal expansion.[1] Functionally graded materials (FGMs) satisfy this requirement. Graded materials have properties which vary as a function of position.[2,3] Continuous changes in the properties of FGMs for instance: chemical composition, grain size, porosity, etc., result in the gradient of the features such as: dielectric, ferroelectric, piezoelectric, magnetic, mechanical strength and thermal conductivity. During the last two decades, after the pioneer works on FGMs for structural applications (thermal barrier and stress relief materials[2]), more uses have been worked out, mostly focused on electronic and functional applications. FGMs have been used for the fabrication of various technological components, such as electrical devices,[4] electrochemical ones,[5] as well as biomaterials.[6] Nowadays, FGMs are established as an attractive class of materials in which it is possible to create a gradient of properties that cannot be attained in any spatially-homogeneous materials.

The concept of FGMs has been used to produce barium titanate stannate ($BaTi_{1-x}Sn_xO_3$, BTS) electronic devices.[7,8] Due to high dielectric permittivity in a wide temperature range and lead-free relaxor behavior, BTS FGMs have practical and/or potential application in electronic industry as: ceramic capacitors, bending actuators,[7] microwave phase shifters,[9] sensors,[10] etc. The electrical characteristics of the BTS FGMs, i.e. dielectric permittivity, position of $\varepsilon_{r,max}$ at the temperature scale, and width of Curie temperature intervals, can be tailored by modifying Ti/Sn concentration gradient.[8]

Primarily, an important processing goal for FGMs is to obtain a high-quality microstructure with desired grain size and density. During the thermal treatment, different graded layers in a FGM show different shrinkage kinetics, i.e. different shrinkage rates and extents of shrinkage during sintering, as well as different final density.[11] This phenomenon can lead to excessive shape distortion, warping, delamination, development of cracks and microstructural damage in the sintered FGMs. Therefore, for the processing of BTS FGMs, it is desirable to choose appropriate BTS ingredients which will produce the desired Ti/Sn concentration gradient and electrical characteristics, certainly without micro- and/or macrostructural damages.

In the present study, the BTS ingredient materials were first synthesized and their main characteristics were examined. According to dielectric characteristics of the BTS ingredients, several different Ti/Sn concentration gradients were chosen and functionally graded barium titanate stannate materials were fabricated by the powder processing followed by sintering. Furthermore, the influence of the concentration gradient on electrical characteristics was studied using *IS*. The grain-interior and grain boundary contributions in BTS FGMs were

separated; activation energies were calculated for both of them. Finally, microstructural and/or macrostructural defects of FGMs were investigated by *IS*, SEM and thermal microscopy.

EXPERIMENTAL PROCEDURE

(a) BTS ingredients

The initial BTS powders ($BaTi_{1-x}Sn_xO_3$, with nominal composition x = 0.025, 0.05, 0.07, 0.10 and 0.15, marked as BTS2.5, BTS5, BTS7, BTS10, and BTS15, respectively) were prepared by a conventional solid state reaction. The starting materials were commercially available $BaCO_3$ (>99%), TiO_2 (rutile, >99.8%) and SnO_2 (>99%). Stoichiometric mixtures of $BaCO_3$, TiO_2 and SnO_2 powders were homogenized in ethanol for 24 h by stirring with a magnetic stirrer. The obtained powder slurries were dried and calcined at 1100 °C for 1 h. Particle size distribution (d_{50}) was measured by laser particle size analyzer. The used instrument was Mastersizer 2000 (Malvern Instruments Ltd., UK).

For further analyses the BTS powders were pressed and sintered at the same conditions as FGMs later (1420 °C, for 1h). Before they were pressed into pellets, the calcined BTS powders were crushed and triturated in agate mortar in 2-propanol in order to ensure particle size uniformity. The phase analysis and crystal structure of the BTS powders were determined at room temperature, using a powder X-ray diffractometer (Philips PW 1050, Cu $K\alpha_{1,2}$ radiation, at 40 kV and 20 mA). The samples for XRD analysis were crushed and powdered in agate mortar in chlorophorm in order to minimize the effects of the preferred orientation. The diffraction measurements were done over a scattering angle 2θ from 20 to 120° with a step of 0.02° and a counting time of 15 s. Rietveld analysis on the XRD patterns was carried out using the FullProf software package. JCPDS database was used for phase identification.[12] The theoretical density of the BTS powders was calculated according to the Rietveld analysis on the XRD data. The main properties of the BTS powders are given in Table 1.

Raman spectroscopy investigations of BTS ingredients were carried out at room temperature, by a Raman System R-2001 Spectrometer, equipped with a linear silicon CCD detector. The samples were excited using a red solid-state diode laser at 785 nm. The Raman spectra were recorded in the frequency interval 200-2000 cm^{-1}.

The dielectric permittivity of the BTS ingredients was studied as a function of temperature. The measurements were done on sintered pellets electroded with silver paste. The measurements were performed on air, at 1 kHz (internal frequency) using a Wayne Kerr Universal Bridge B224. All dielectric measurements were done during cooling from 170 to −15 °C.

(b) FGMs

The FGMs with different Ti/Sn concentration gradients were fabricated by the powder stacking method. The BTS powders with the preferred stoichiometry were stacked sequentially in die (∅ 6 mm); the combinations of powders were: 2.5/15; 2.5/5/7; 15/5/7 and 2.5/5/7/10 (the numbers denote mol% of Sn in BTS); each layer had the thickness *circa* 800 μm. Multilayered compacts were uniaxially pressed under a pressure of 300 MPa. The samples were sintered in Protherm tube furnace, in air, at a heating rate of 10 °/min up to 1420 °C, the duration of the isothermal sintering was 1 h.

The impedance spectroscopy (*IS*) analysis was performed on a Gamry EIS300 Impedance Analyzer at frequencies of 1 Hz-100 kHz. Measurements were done in air during cooling from 320 to 25 °C; the applied voltage was 100 mV. As electrodes, high conductivity silver paste was applied onto both sides of the samples, parallel to the layers. During the measurement, samples were put in an adequate holder placed in a muff oven. A Pt-Rh thermocouple located in a hot-sample holder was used for temperature monitoring. The impedance data were fitted by software *Z*-View2 (version 2.6 demo). All of the impedance data collected between 320 and 25 °C were normalized by multiplying by the geometrical factor g [cm], which yielded the specific resistivity ρ [Ω·cm]. The geometrical factor was estimated for every singe sample from its geometry (g is defined as A/d, where A is the sample area and d the thickness of the sample). The data were cut at the low frequency end (between 1 and 4 Hz) in order to avoid the fitting of the sample response dominated by noise.

The microstructure of the FGMs was analyzed using a scanning electron microscope (SEM, JEOL JXA-840A) equipped with an energy-dispersive spectrometer (EDS, Tracor Northern, NORAN, Series II). In order to assess the gradient profile of the FGMs, the samples were cut perpendicularly with respect to the layers. EDS

analyses were done on the polished cross-sectional surfaces, while, for the SEM analyses samples were additionally thermally etched at 1320 °C for 10 min. Before the measurements, the FGMs were carbon coated.

Finally, in the aim of the *in situ* monitoring of the FGMs' macrostructural deformation (cracks, delamination, distortion, etc.) during the sintering, the most complex 2.5/5/7/10 sample was sintered in a heating microscope (New Heating Microscope EM201, Hesse Instruments, Germany). The experiment was performed under the same conditions as previously in a classical furnace.

RESULTS AND DISCUSSION

(a) BTS ingredients

It is well known that the characteristics of the starting powders influenced the quality (furthermore the electrical properties) of the final ceramics. Precisely, for the preparation of dense ceramics with excellent dielectric properties, sub-micro or nano-sized powders with uniform particle size are required.[13,14] These are the reasons why we at first examined the average particle size of the starting BTS powders. As example, Fig. 1 shows the particle size distribution of the BTS2.5 powders; the values of the average particle size of all the BTS powders are listed in Table 1. We noticed that all of the powders were sub-micro-sized, with the average particle size d_{50} of nearly 250 nm; the powders were uniform with narrow particle size distributions (*span* < 1).

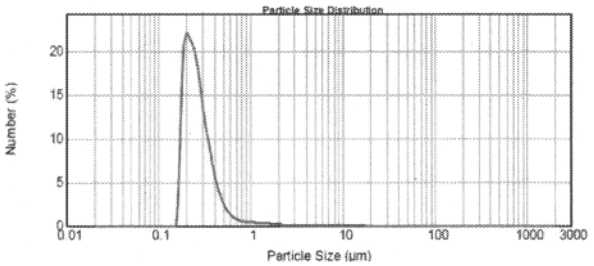

Fig. 1 Particle size distribution (based on number) for BTS2.5 powder.

Furthermore, we examined the properties of the BTS ingredients sintered in the same conditions as the FGMs later (1420 °C, 1 h). This is the first step towards tailoring BTS FGMs since the properties of the ingredients will be repercuted on the characteristics of the final FGMs. We first characterized the crystal structure of the BTS ingredients. Fig. 2(a) shows the XRD patterns of the BTS powders obtained after the sintering. We found that all of the samples were crystallized into single-phase solid solutions of perovskite structure. From Fig. 2(a), it can be observed that the increasing of Sn content causes systematic shift of reflections towards lower 2θ angles, because the substitution of Ti^{4+} [$R(Ti^{4+})$ = 74.5 pm] by Sn^{4+} [$R(Sn^{4+})$ = 83.0 pm][15] increases the d spacing. This is a clear indication that Sn^{4+} is systematically dissolved in the $BaTiO_3$ lattice in the studied composition range. With increasing of Sn content, the crystal structure of BTS ingredients becomes less and less tetragonal, and finally shows cubic structure for the BTS sample with 15 mol% of Sn.

The appearance of only tetragonal ($0.025 \leq x \leq 0.10$) and cubic ($x=0.15$) phases is not in accordance with the reports on the existence of orthorhombic ($0.025 \leq x \leq 0.075$) and rhombohedral ($0.075 \leq x \leq 0.15$) phases,[16,17] but it is in accordance with the study of W.-K. Cheng *et al.*[18] We suppose that the absence of orthorhombic and rhombohedral phases is probably a consequence of the tetragonal phase stabilization caused by the samples preparation method (high temperature solid state reactions). The magnifier change of the most characteristics reflection of the BTS XRD patterns, the (200) reflection, with tin content is shown in Fig. 2(b).

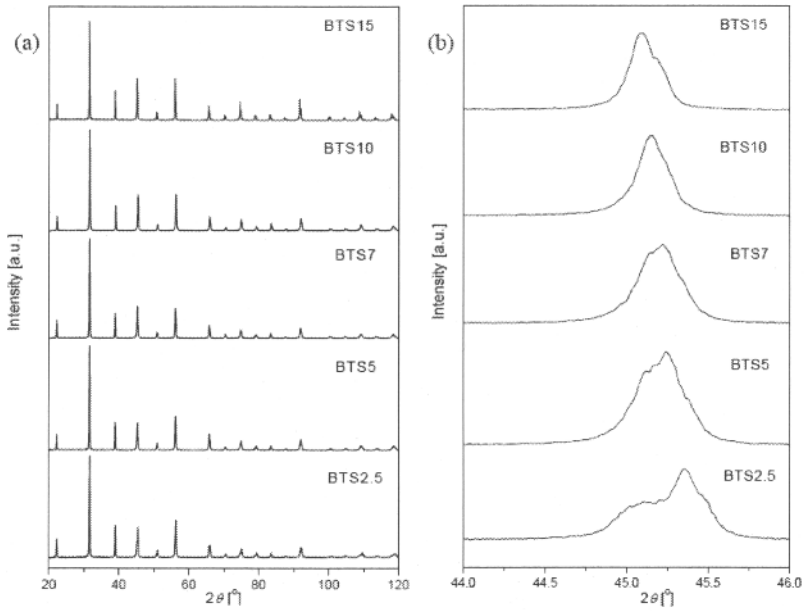

Fig. 2 (a) XRD patterns of the BTS powders sintered at 1420 °C for 1 h, and (b) the change in the (200) reflection (~ 45° 2θ) with x = 0.025, 0.05, 0.07, 0.10 (tetragonal phases) and 0.15 (cubic phase).

Table 1 Characteristics of used BTS powders.

	BTS2.5	*BTS5*	*BTS7*	*BTS10*	*BTS15*
Nominal stoichiometry	$BaTi_{0.975}Sn_{0.025}O_3$	$BaTi_{0.95}Sn_{0.05}O_3$	$BaTi_{0.93}Sn_{0.07}O_3$	$BaTi_{0.9}Sn_{0.10}O_3$	$BaTi_{0.85}Sn_{0.15}O_3$
Crystal structure	Tetragonal	Tetragonal	Tetragonal	Tetragonal	Cubic
*T.D. (g/cm^3)	6.06	6.10	6.14	6.19	6.22
**d_{50} (nm)	250	250	250	250	250

*, ** Here it can be emphasized that the values of the average particle size and theoretical density (T.D.) are important because they determine the activation energy for the sintering process of the ingredients, precisely, they determine the shrinkage behavior of every single layer in FGMs during sintering.

One more technique is used to confirm the phase identification of BTS powders, as well, the absence of orthorhombic and rhombohedral phases. The Raman spectroscopy is an excellent complimentary characterization tool to identify the phase evolution as a function of Sn substitution in the barium titanate lattice because tetragonal BT has the Raman active crystal symmetry of C_{4v}^1, showing distinguishable Raman peaks at room temperature, in contrast to cubic BT with the Raman inactive O_h^1 symmetry, leading to the peak disappearance.

Fig. 3 presents the Raman spectra of the BTS ingredients, while the band assignments and band positions are given in Table 2.

In the Raman spectrum of BTS2.5 (Fig. 3), the bands at about 270 and 510 cm^{-1} are assigned to the transverse optical (TO) modes of A_1 symmetry, whereas the peak at about 300 cm^{-1} corresponds to the B_1 mode. The weak peak at 711 cm^{-1} is related to the longitudinal (LO) mode of A_1. They are typical peaks in the Raman spectrum of the tetragonal BT phase.[19] It is known that the peaks at around 305 and 715 cm^{-1} are characteristic of the tetragonal phase and disappear when the barium titanate structure is cubic.[20] Thus, the Raman spectrum of the cubic barium titanate phase has only two bands, at 270 and 510 cm^{-1}. This means that it is possible to distinguish the cubic and the tetragonal phase of barium titanate-based materials on the basis of a Raman spectrum.

Some changes in the evolution of the Raman spectra with Sn substitution on Ti sites can be seen in Fig. 3. The Raman spectra are changed gradually from BTS2.5 to BTS15. The 300 cm^{-1} peak becomes less sharp, even indistinct, when the tetragonal phase is not dominant. Two broad bands at 280 and 506 cm^{-1} in the Raman spectrum of BTS15 confirmed the existence of the cubic symmetry, moreover, the weak peak at near 715 cm^{-1} indicates a small amount of tetragonal phases, which was not observed by XRD. As in the case of the XRD examinations, the existence of the orthorhombic and/or rhombohedral phases was not identified with Raman spectroscopy either.

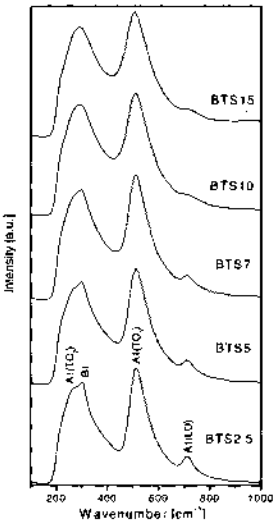

Fig. 3 Raman spectra of BTS ingredients sintered at 1420 °C.

Table 2 The assignment and positions of bands in the Raman spectra of BTS sintered at 1420 °C.

BTS ingredients	Bands assignment and positions (cm^{-1})			
	TO_2 mode of A_1	B_1 mode	TO_3 mode of A_1	LO mode of A_1
BTS2.5	270	301	512	711
BTS5	270_{sh}	300	510	711
BTS7	270	300_{sh}	510	710
BTS10	280	/	509	720_{sh}
BTS15	280	/	506	730_{sh}

The next section of the paper deals with the temperature-dependent dielectric permittivity of the BTS ingredients recorded at the fixed frequency of 1 kHz. The permittivity measurements at the frequency of 1 kHz give information significant for practical applications of barium titanate-based ceramic materials.[21]

Fig. 4 presents the temperature dependence of the dielectric permittivity for the BTS ingredients sintered at 1420 °C. It can be seen that as the substitution of Ti^{4+} by Sn^{4+} ions increases, from 2.5 up to 15 mol%, the maximum of the dielectric constant increases too, followed by broadening; while the cubic to tetragonal transition temperature (Curie temperature, T_c) decreases. It can be seen that the values of ε_{max} are in the range from 6000 to 9000; also, Sn substitution on Ti sites increased the room-temperature dielectric constant from about 1100 for BTS2.5 up to 5000 for both BTS10 and BTS15. For Sn amount lower than 10 mol%, the BTS ceramics show conventional ferroelectric properties, with two phase transitions: cubic to tetragonal (T_c) and tetragonal to orthorhombic (T_1). With increasing of the Sn content, both the two transition points and the corresponding ε_r maxima become closer and coalesce at near 10 mol% into a single broad maximum (Fig. 4). The notable broad Curie maximum is an implication of the diffuse phase transition behavior. So, the substitution of Sn into Ti sites leads to a crossover from sharp to a diffuse phase transformation when the Sn content was in the range 2.5 to 15 mol% (Fig. 4). The transition temperatures T_c and T_1 for the sintered BTS ingredients are marked in Fig. 4.

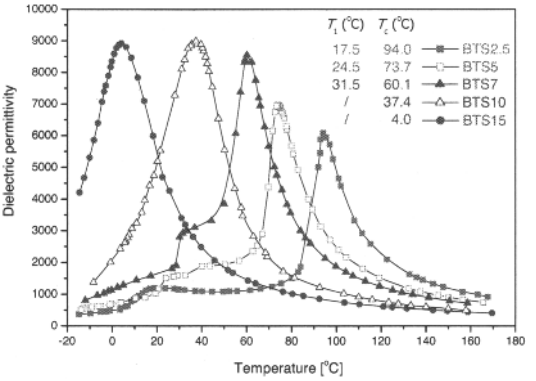

Fig. 4 The temperature dependence of the dielectric permittivity of the BTS ingredients sintered at 1420 °C.

(b) BTS FGMs

It has been shown that the BTS ceramics have a high dielectric constant, unfortunately in narrow temperature intervals. The Curie temperature intervals can be broadened by producing of FGM devices.[8,22] In Fig. 5, the dielectric permittivity of the 2.5/15 and 2.5/5/7/10 FGMs are shown. These two samples are selected as examples of the stepped and continuous Ti/Sn concentration gradient in FGMs, respectively. It can be seen that the 2.5/15 FGM, with a stepped concentration gradient, has two separate Curie temperature intervals and, thus, it is not appropriate for producing capacitors applicative in wide temperature intervals. Contrary, the 2.5/5/7/10 FGM, with a continuous Ti/Sn concentration gradient, has a relatively high dielectric constant in a wide temperature range; also, its maximum of dielectric permittivity is broadened and relatively flattened compared to those of the BTS. Such an electrical characteristic can ensure an effective application of capacitors in the wide temperature range. The importance of the FGMs technology rest in the fact that enable the tailoring of capacitors with desirable width (and positions on T axis) of the Curie temperature intervals by choosing the concentration gradient. Certainly, the maximum of dielectric permittivity is determined by the nature of materials (in this case BTS) and significantly by the created microstructure.

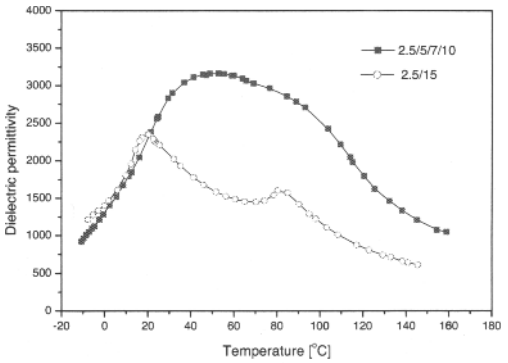

Fig. 5 The temperature dependence of the dielectric constant in the BTS FGMs sintered at 1420 °C for 1 h.

The microstructure (average grain size, density and grain boundaries) of ceramic materials influences their electrical characteristics. For electronic ceramics, the grain boundary resistivity is especially important since grain boundaries act as barriers for the cross transport of the charge carriers and consequently prevent leakage currents through electronic components. The above-presented fixed–frequency measurements are insufficient to determine electrical properties of the grain boundaries in FGMs; therefore, we used impedance spectroscopy (*IS*) to examine the influence of the concentration gradient on electrical characteristics (especially resistivity) of the bulk and grain boundaries separately. Furthermore, we determined the activation energies for the bulk and grain boundary ionic conductivity for different FGMs. Finally, potential macrostructural defects (delamination and/or cracks), which may be a serious problem during the fabrication of FGMs by powder processing and sintering, were checked with the aid of *IS*.

Impedance spectroscopy is an accurate, non-destructive technique for the characterization of bulk materials, and other unspecific phases such as secondary phases, porosity, cracks, etc. Moreover, *IS* is a powerful technique enabling to distinguish the grain-interior and grain boundary resistance contributions of many oxide ceramics with ionic or mixed ionic/electronic conduction.

A typical complex impedance diagram, in the so-called Nyquist presentation (the plot of imaginary, Z'', *versus* real impedance, Z', with the frequency f as an independent parameter) of a sintered, low-conducting material between blocking electrodes, consists of three parts, ending at the origin point of coordinate system at infinite frequency. For sintered barium titanate-based materials, the high-frequency semicircle of the impedance spectra is attributed to the grain-interior impedance, the middle one is attributed to the grain boundary response, whereby the low-frequency arc (<0.1 Hz) corresponds to the electrode response.[21,23] The grain-interior and grain boundary resistance may be read as the diameter of appropriate arcs.

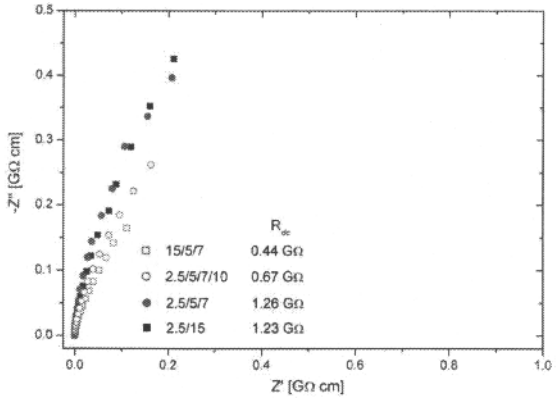

Fig. 6 Impedance spectra of the BTS FGMs recorded at room temperature.

Fig. 6 shows the impedance spectra of BTS FGMs measured at room temperature; it is observed that the shape of Nyquist plots follows a line with a large slope, without point dissipation, indicating high-quality ceramics. This is especially important for FGMs, meaning no insulator interfaces (cracks and/or delamination) between graded layers were produced during powder processing and high-temperature sintering. The estimated direct current specific resistivities, ρ_{dc}, of the FGMs have the values of 10^9 Ω·cm (noted at Fig. 6). Thus, high specific resistivity of the BTS FGMs at room temperature (indicating low leakage currents) in addition to previously determined high relative permittivity in wide temperature intervals make this materials suitable for practical application as capacitors.

Hereafter, in order to separate grain and grain boundary contribution of the ceramics specific resistivity, the *IS* data recorded above T_c (when grain boundary resistivity decreases from 10^{10} to 10^6 Ω) were analyzed.

Fig. 7 shows the impedance spectra of the 2.5/5/7/10 FGM at temperatures between 320 and 210 °C. For clarity's sake, *IS* for chosen temperatures are shown in Fig. 7. The low frequency arc was not found at < 230 °C, which may be due to the effect of the electrode relaxation process overlapping with the grain boundary relaxation process. However, with the increase of temperature (≥ 230 °C) the impedance spectra for all the samples contained two semicircles; the high-frequency one is ascribed to grain-interior resistance, ρ_{gi}, while the low-frequency one is ascribed to grain boundary resistance, ρ_{gb}. From Fig. 7 it can be seen that the shape of Nyquist plots depends on temperature, with a clear increase of grain-interior as well as grain boundary resistivity with decreasing temperature.

The impedance spectra of all the investigated FGMs are very similar, showing the same trend. To be more specific, at temperatures between 320 and 230 °C all the impedance spectra exhibit two semicircles; in addition, the resistivity of grain-interior and grain boundary increase with decreasing temperature.

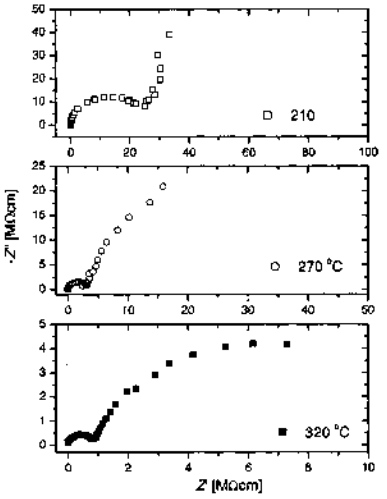

Fig. 7 IS of 2.5/5/7/10 FGM sintered at 1420 °C.

In the next step, the recorded *IS* spectra were fitted by equivalent circuit in computer program Z-View2. In order to achieve this, it was necessary to find appropriate physics-based mathematical model for fitting. For every single impedance spectra it is always possible to find more than one equivalent circuit model that can fit the data. Usually, in the case of polycrystalline materials, the complex impedance diagram in the form of two adjacent arcs, ascribed to the grain-interior and grain boundary relaxation phenomena can be described by an equivalent circuit consisting of two parallel resistor (*R*) and capacitor (*C*) elements connected in series.[21,24] So, as it can be expected, we first fitted the *IS* spectra with two parallel *RC* equivalent elements connected in series. Fig. 8 shows an example of measured impedance data (full squares) additionally fitted (dotted curve) with *RC*-*RC*. Obviously, mismatch exists, meaning that *RC*s are not appropriate for fitting of BTS FGMs. The mismatching can be explained by the following: *RC*s mathematical model is valid for "ideal" systems, where the Nyquist plot is composed from semicircles with the centers on the *x*-axis. However, the observed plots of the BTS FGMs at temperatures above the ferroelectric–paraelectric transition were indeed the arcs of circles, but with the center on some distance below the x-axis. In order to fit these real system impedances, we replaced the capacitor with constant phase element (*CPE*) to account for non-Debye behavior. When, instead of a *C*, a *CPE* is placed in parallel to a resistor, a depressed semi-circle is produced. The existence of depressed semicircles in impedance spectra can be explained by a number of phenomena, depending on the nature of the investigated system. One of the physical explanations for *CPE* behavior is electrode (or surface) roughness; a rough or porous surface can cause a double-layer capacitance to appear as a *CPE*.[25] Another explanation is inhomogeneous reaction rates on a surface.[26] Both might be seen at polycrystalline surfaces (in our case too, having in mind that Ag electrodes were used). Another possible explanation for depressed semi-circles of impedance spectra may be the varying samples' thickness or composition.[27] The last undoubtedly matches with our case, where chemical composition varied throughout the thickness of FGM. One more reason for the *CPE* behavior is non-uniform current distribution.[28]

Accordingly, to represent the impedance properties of the BTS FGMs at temperatures above the ferroelectric–paraelectric transition, an equivalent circuit consisting of two parallel *RCPE* elements connected in series (Fig. 8) was proved to be appropriate. The measured impedance data (full squares) additionally fitted

(solid curve) with *RCPE* equivalent circuits is shown in Fig. 8. Good match between the recorded and fitted data can be observed. After the fitting, ρ_{gi} and ρ_{gb} were obtained as output from *Z*-View2 computer program. Furthermore, these values of specific resistivities [Ω·cm] were converted to specific conductivities [S·cm^{-1}] and used for the calculation of activation energies, separately for the grain-interior and grain boundary conductivity. For microcrystalline, barium titanate-based materials, at higher temperatures, the total conductivity determined by *IS* can be ascribed to the mixed (ionic and electronic) conductivity. It can be pointed out that at temperatures above T_c the electronic conductivity is significantly smaller than the ionic conductivity. Total ionic conductivity can be related to a migration energy or mobility barrier for oxygen vacancies.

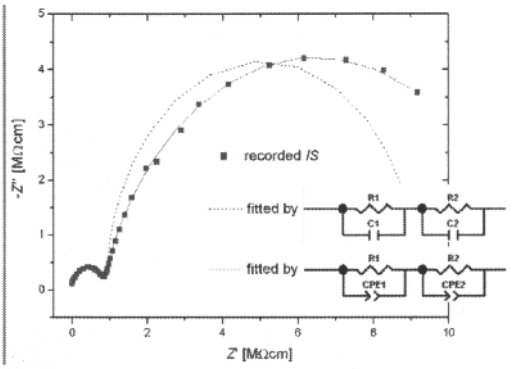

Fig. 8 An example of the measured (an 2.5/5/7/10 FGM at 320 °C) and additionally fitted impedance spectrum. Equivalent circuits used for fitting the IS data are presented.

The experimental data for total ionic conductivity were fitted as a function of temperature *T* following the Arrhenius law:

$$\sigma = (\sigma_0/T)\exp(-E_a/k_BT) \qquad (1)$$

where E_a is the activation energy for ionic migration, k_B is the Boltzmann constant, and σ_0, the pre-exponential factor, is a constant related to the density of charge carriers. Total ionic conductivity can be separated on grain-interior ($\sigma_{gi} = 1/\rho_{gi}$) and grain boundary ($\sigma_{gb} = 1/\rho_{gb}$) contribution.

Arrhenius plots of grain-interior and grain boundary conductivity, for BTS FGMs are shown in Fig. 9. All obey the Arrhenius law and therefore activation energies (separately E_{gi} and E_{gb}) can be estimated from the slopes of these diagrams. The values of the activation energies determined by the least square fitting of the specific conductivity data are noted in the Fig. 9.

It is known that the activation energy for the grain interior conductivity (E_{gi}) is determined by chemical composition. In the case of BTS FGMs, E_{gi} vary in the range from 0.74 to 0.78 eV, keeping the intrinsic properties of BTS.[29,30] Thus, we determined that E_{gi} of FGMs does not depend on the concentration gradient. Contrary, the activation energy for the grain boundary conductivity, E_{gb}, is ruled by the ceramics microstructure, as well as by electrical inhomogeneity in the region of the necks between grains. Here, E_{gb} of the FGMs, with different Ti/Sn concentration gradient, varies in the range of 1.03 to 1.29 eV. The highest E_{gb} of 1.29 eV, exhibits FGM 2.5/15, the material with stepped concentration gradient, which has the highest concentration/inhomogeneity and microstructural/porosity gradient. Air gaps on the contact between grains of different stoichiometry were produced due to different theoretical density of the used powder, so, high-porosity gradient is produced in applied sintering conditions. These inhomogeneities and air gaps act as potential barriers for oxygen ions transport. Accordingly, FGM 15/5/7 with the smallest concentration (and inhomogeneity), microstructural and porosity gradient, has the smallest E_{gb} (1.03 eV). Therefore, E_{gb} is influenced by microstructural/porosity gradient, which are direct consequences of the concentration gradient. Precisely, it is deduced that an increase of concentration gradient promotes the increase of potential inhomogeneity, microstructural and porosity gradients, as well as an increase of E_{gb}.

The associated relaxation time, ($\tau = (2\pi f_{max})^{-1}$, where f_{max} is the frequency at the top of the Z'' *vs.* Z' arcs)[23] for grain interior (τ_{gi}) and grain boundary (τ_{gb}), was also determined. The relaxation time is a geometry and microstructure independent parameter; but, depends merely on the intrinsic conductivity of a material.[31] We found that for the studied FGMs τ_{gi} is almost identical. The calculated values, for temperatures interval from 320 to 230 °C, fall in the range of 10^{-6} to 10^{-4} s, respectively. Besides, the calculated values for τ_{gb} are from 10^{-3} to 10^{0} s. Obviously, the grain boundary relaxation times are about three orders of magnitude larger than those of the grain interior. As expected, in the grain boundary structure the time spent in the relaxation process is longer.

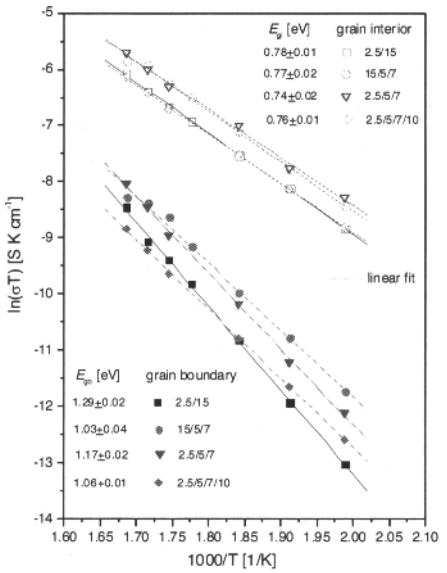

Fig. 9 Arrhenius plots of ln(σT) versus 1000/T of the FGMs with different concentration gradient. The contributions of grain interior and grain boundary are separated. Estimated activation energies are marked.

Previously, we have been used a heating microscope, as an optical dilatometer, for detailed quantitative studies of the sintering kinetics of each layer in FGMs.[11] Here, we used a heating microscope for *in situ* qualitative monitoring of the FGMs' microstructure during the sintering; naturally, the sintering was done in the same conditions as previously in the tube furnace. The photographs of 2.5/5/7/10 FGM during sintering in a heating microscope, at tree representative temperatures ((a) at the beginning of sintering regime, (b) at the start of the shrinkage, and (c) at the end of the sintering regime) are shown in Fig. 10. It can be emphasized that during the sintering process macrostructural damages were not observed.

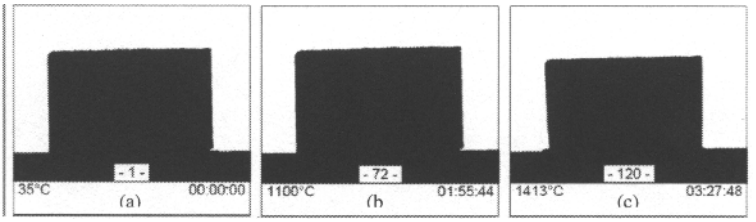

Fig. 10 Photographs of 2.5/5/7/10 FGM during sintering, as observed in heating microscope, at (a) room temperature, (b) 1100 °C and (c) 1420 °C.

According to the results of *IS*, and due to the *in situ* monitoring of 2.5/5/7/10 FGM during sintering, delamination or distortion of the FGM does not exist. These assumptions were confirmed by a SEM analysis of 2.5/5/7/10 FGM in cross-sectional view, as shown in Fig. 11. It can be seen that there is no distinct boundary between the graded layers in the FGM (Fig. 11 (a)). Clearly, delamination or distortion of FGMs does not exist. Figs. 11 (b) and (c), shows the magnifier BTS10 and BTS2.5 regions, respectively. Some change in the

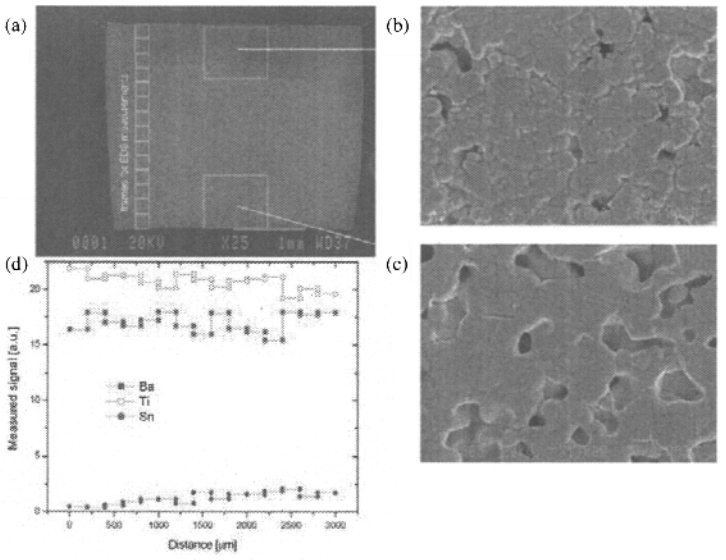

Fig. 11 (a) SEM image of the macroscopic cross-section shape of BTS2.5/BTS5/BTS7/BTS10 FGM, (b)-(c) magnifier BTS10 and BTS2.5 regions, respectively, and (d) distribution of ions through the FGM measured with semi-quantitative frame by frame EDS analyses. Positions of the analyses are shown in Fig. 11 (a).

microstructure, precisely, in the average grain size and density, can be observed. The bottom part, with the smaller amount of tin, has larger grains and higher open porosity than the upper part of the FGM, which has a higher amount of tin. This fact is yet another evidence of the gradients in the microstructure and porosity. Moreover, the existence of the Ti/Sn concentration gradient is approved by semi-quantitative "frame by frame" EDS analyses, Fig. 11 (d).

We have previously shown that regardless the heating rate during the sintering, there is always a difference in shrinkage between graded layers in BTS FGMs; precisely, the BTS2.5 graded layer in FGMs always reaches higher values of shrinkage than the graded layers with a higher content of tin.[11] Generally, sintering shrinkage depends on composition, green density, temperature, time, atmosphere, etc.[32] Here, the different sintering shrinkage of the graded layers in the 2.5/5/7/10 FGM is attributed to the difference in the tin content (composition), and can be explained by a different activation energy for the sintering of the BTS ingredients. This fact causes the cone-shaped FGM (Fig. 11 (a)).

CONCLUSION

Barium titanate stannate ($BaTi_{1-x}Sn_xO_3$, BTS) powders were synthesized by solid state reaction. The main characteristics of the powders and sintered ceramics were analyzed with the aim of tailoring functionally graded materials (FGMs).

BTS FGMs with several different Ti/Sn concentration gradients (2.5/15, 2.5/5/7, 2.5/5/7/10, and 15/5/7; numbers denote mol% of Sn in BTS) were prepared by powder processing followed by sintering. The dielectric permittivity of the prepared FGMs was determined. It was shown that dielectric permittivity of FGMs depends on the Ti/Sn concentration gradient. Precisely, FGMs with the stepped concentration gradient have separated and narrow Curie temperature intervals; contrary, the FGMs with continual Ti/Sn concentration gradient, have a relatively high dielectric constant in a wide temperature range, with broadened and relatively flatted maximum of dielectric permittivity.

Additionally, the influence of Ti/Sn concentration gradient on electrical characteristics of the FGMs was examined by impedance spectroscopy (*IS*). The grain-interior and grain boundary resistivity of the FGMs were distinguished and activation energies were calculated. It was established that for FGMs the activation energy deduced from the grain-interior conductivity is defined by chemical composition (intrinsic property) and does not depend on the concentration gradient. Quite contrary, the activation energy for the grain boundary conductivity is determined by the microstructural gradient which is a direct consequence of the concentration gradient.

Finally, microstructural and/or macrostructural defects of FGMs were investigated by *IS*, SEM and thermal microscopy. According to the results of *IS* obtained at room temperature, direct current specific resistivities of the FGMs were estimated. The values of 10^9 Ω·cm point to high specific resistivity of the BTS FGMs at room temperature as well as low leakage currents. These results indicate that there are no insulator interfaces (cracks and/or delamination) between the graded layers in FGMs. This assumption was confirmed by *in situ* monitoring of the sintering processes in a thermal microscope, and furthermore, by a SEM analysis of the FGMs in cross-sectional view.

So, it was shown that FGMs technology enables us to tailor ceramic materials with desirable electrical characteristics (the width of the Curie temperature intervals and their positions on the temperature scale, grain boundary resistivity) by choosing the appropriate concentration gradient. What's more, the use of submicron-powders with similar both, average particle size and theoretical densities, ensure the creation of the FGMs free from micro- and macro-structural damages.

ACKNOWLEDGEMENT

The Ministry of Science and Technological Development of the Republic of Serbia provided financial support under Grant No. 142006. The SEM and EDS results are preliminary and will be published later. These results were obtained at Jožef Stefan Institute in Ljubljana, Slovenia, owing to the bilateral cooperation program between the Republic of Serbia and the Republic of Slovenia. The authors would like to thank to Prof. Dr. Danilo Suvorov and Dr. Srečo Škapin for their support.

REFERENCES

1 A. J. Sánchez-Herencia, R. Moreno, and J. R. Jurado, 'Electrical transport properties in zirconia/alumina functionally graded materials', *J. Eur. Ceram. Soc.*, **20**, 1611–20 (2000).

2 M. Koizumi, and M. Nino, 'Overview of FGM research in Japan', *MRS Bull.*, **20**, 19-21 (1995). (Special Issue, Functionally Gradient Materials, Edited by E. L. Fleitscher).

3 B. Kieback, A. Neubrand, and H. Reidel, 'Processing techniques for functionally graded materials', *Mater. Sci. Eng. A*, **362**, 81-106 (2003).

4 C. C. Wu, M. Khan, and W. Moy, 'Piezoelectric ceramics with functional gradient: a new application in material design', *J. Am. Ceram. Soc.*, **79**, 809-12 (1996).

5 Z. Liu, M.-F. Han, and W.-T. Miao, 'Preparation and characterization of graded cathode $La_{0.6}Sr_{0.4}Co_{0.2}Fe_{0.8}O_{3-\delta}$', *J.Power Sources* **173**, 837-41 (2007).

6 V. Thomas, X. Zhang, S. A. Catledge, and Y. K. Vohra, 'Functionally graded electrospun scaffolds with tunable mechanical properties for vascular tissue regeneration', *Biomed. Mater.*, **2**, 224-32 (2007).

7 R. Steinhausen, A. Kouvatov, H. Beige, H. T. Langhammer, and H-P. Abicht, 'Poling and bending behavior of piezoelectric multilayers based on $Ba(Ti,Sn)O_3$ ceramics', *J. Eur. Ceram. Soc.*, **24**, 1677-80 (2004).

8 S. Marković, M. Mitrić, N. Cvjetićanin, and D. Uskoković, 'Preparation and properties of $BaTi_{1-x}Sn_xO_3$ multilayered ceramics', *J. Eur. Ceram. Soc.*, **27**, 505-9 (2007).

9 W. Xiaoyong, F. Yujun, and Y. Xi, 'Dielectric relaxation behavior in barium stannate titanate ferroelectric ceramics with diffused phase transition', *Appl. Phys. Lett.*, **83**, 2031-3 (2003).

10 E. Müller, Č. Drašar, J. Schilz, and W. A. Kaysser, 'Functionally graded materials for sensor and energy applications', *Mater. Sci. Eng. A*, **362**, 17-39 (2003).

11 S. Marković, and D. Uskoković, 'The master sintering curves for $BaTi_{0.985}Sn_{0.025}O_3/BaTi_{0.85}Sn_{0.15}O_3$ functionally graded materials', *J. Eur. Ceram. Soc.*, **29**, 2309-16 (2009).

12 *JCPDS Database on CD-ROM*. Newton Square, PA: International Centre for Diffraction Data; 1999.

13 P. Pinceloup, C. Courtois, A. Leriche, and B. Thierry, 'Hydrothermal synthesis of nanometer-sized barium titanate powders: Control of barium/titanium ratio, sintering, and dielectric properties', *J. Am. Ceram. Soc.*, **82**, 3049-56 (1999).

14 Z. Zhao, V. Buscaglia, M. Viviani, M. T. Buscaglia, L. Mitoseriu, A. Testino, M. Nygren, M. Jonhsson, and P. Nanni, 'Grain-size effects on the ferroelectric behavior of dense nanocrystalline $BaTiO_3$ ceramics', *Phys. Rev. B*, **70**, 024107-1-8 (2004).

15 R. D. Shannon, and C. T. Prewitt, 'Effective ionic radii in oxides and fluorides', *Acta. Cryst.*, **B25**, 925-46 (1969).

16 N. Yasuda, H. Ohwa, and S. Asano, 'Dielectric properties and phase transitions of $Ba(Ti_{1-x}Sn_x)O_3$ solid solution' *Jpn. J. Appl. Phys.*, **35**, 5099-103 (1996).

17 V. Müller, H. Beige, H.-P. Abicht, and C. Eisenschmidt, 'X-ray diffraction study revealing phase coexistence in barium titanate stannate', *J. Mater. Res.*, **19**, 2834-40 (2004).

18 W.-K. Chang, S.-F. Hsien, Y.-H. Lee, K.-N. Chen. N.-C. Wu, and A.A. Wang, 'X-ray diffraction studies of phase transformations between tetragonal and cubic phases in the $BaSn_xTi_{1-x}O_3$ system', *J. Mat. Sci.*, **33**, 1765-8 (1998).

19 M. DiDomenico, S. H. Wemple, S. P. S. Porto, and R.P. Bauman, 'Raman spectrum of single-domain $BaTiO_3$', *Phys. Rev.*, **174**, 522-30 (1968).

20 S. W. Lu, B. I. Lee, Z. L. Wang, and W.D. Samuels, 'Hydrothermal synthesis and structural characterization of $BaTiO_3$ nanocrystals', *J. Cryst. Growth*, **219**, 269-76 (2000).

21 N. Hirose, and A. R. West, 'Impedance spectroscopy of undoped $BaTiO_3$ ceramics', *J. Am. Ceram. Soc.*, **79**, 1633-41 (1996).

22 S. Marković, M. Mitrić, Č. Jovalekić, and M. Miljković, 'Dielectric and Ferroelectric Properties of $BaTi_{1-x}Sn_xO_3$', *Mat. Sci. Forum*, **555**, 249-254 (2007).

23 'Impedance Spectroscopy', Edited by J. R. Macdonald. John Wiley & Sons; New York, Chichester, Brisbane, Toronto, Singapore, 1987.

24 D. C. Sinclair, and A. R. West, 'Impedance and modulus spectroscopy of semiconducting $BaTiO_3$ showing positive temperature coefficient of resistance', *J. Appl. Phys.*, **66**, 3850-6 (1989).

25 W. H. Mulder, J. H. Sluyters, T. Pajkossy, and I. Nyikos, 'Tafel current at fractal electrodes. Connection with admittance spectra', *J. Electroanal. Chem.*, **285**, 103-15 (1990).

26 C.-H. Kim, S.-I. Pyun, and J.-H. Kim, 'An investigation of the capacitance dispersion on the fractal carbon electrode with edge and basal orientations', *Electrochim. Acta*, **48**, 3455-63 (2003).

27 C. A. Schiller, and W. Strunz, 'The evaluation of experimental dielectric data of barrier coatings by means of different models', *Electrochim. Acta*, **46**, 3619-25 (2001).

28 J.-B. Jorcin, M. E. Orazem, N. Pebere, and B. Tribollet, 'CPE analysis by local impedance analysis', *Electrochim. Acta*, **51**, 1473-9 (2006).

29 S. Marković, Č. Jovalekic, Lj. Veselinović, S. Mentus, and D. Uskoković, 'Electrical properties of barium titanate stannate functionally graded materials', *J. Eur. Ceram. Soc.*, DOI:10.1016/j.jeurceramsoc.2009.10.020

30 X. Wei, and X. Yao, 'Preparation, structure and dielectric property of barium stannate titanate ceramics', *Mater. Sci. Eng. B*, **137**, 184-8 (2007).

31 P. Sooksaen, I. M. Reaney, D. C. Sinclair, 'Crystallization and dielectric properties of borate-based ferroelectric $PbTiO_3$ glass-ceramics', *J. Electroceram.*, **19**, 221-8 (2007).

32 R. M. German, 'Sintering theory and practice'. John Willey & Sons, INC, New York, Chichester, Brisbane, Toronto, Singapore, 1996.